



Carbon spheres supported visible-light-driven CuO-BiVO₄ heterojunction: Preparation, characterization, and photocatalytic properties

Weirong Zhao*, Yan Wang, Yong Yang, Jing Tang, Yanan Yang

Department of Environmental Engineering, Zhejiang University, Hangzhou 310058, China

ARTICLE INFO

Article history:

Received 26 July 2011

Received in revised form

11 December 2011

Accepted 15 December 2011

Available online 23 December 2011

Keywords:

Photocatalysis
Methylene blue
Photodegradation
Photosensitizer
Electron transfer

ABSTRACT

To utilize visible light more effectively in photocatalytic reactions, carbon-supported CuO-BiVO₄ (CuO-BVO@C) composite photocatalyst was prepared by hydrothermal process and impregnation technique. The photocatalytic activities of as-prepared catalysts were evaluated by degradation of methylene blue (MB) in aqueous solution under visible light irradiation, it was found that CuO-BVO@C exhibits the highest photocatalytic degradation activity with the pseudo-first-order rate constant K_a five times higher than pure BiVO₄, which could be assigned to the synergistic effect of CuO-BiVO₄ heterojunction and carbon spheres. The characterization of photocatalysts by a series of joint techniques, including X-ray diffraction, scanning electron microscopy, transmission electron microscopy, UV–vis diffuse reflectance spectra, PL spectra and electrochemistry technology, discloses that carbon spheres play two crucial roles in enhancing of photocatalytic activity. One is to act as a dispersing support to suppress the grain growth, the other is to act as a photosensitizer to transfer the electrons to CuO-BiVO₄ heterojunction, which narrows the band gap of BiVO₄, hinders the electron–hole pair's recombination, extends the absorption range of visible light, and improves the photocatalytic performance of catalyst. The photocatalytic degradation pathways mainly involve the formation and reaction of $\cdot\text{OH}$ radicals. Based on the experimental results of electron spin-resonance spectroscopy, a reasonable mechanism was also proposed to elucidate the role of carbon spheres in the CuO-BVO@C composite as a photocatalyst for degradation of organic pollutants.

© 2011 Elsevier B.V. All rights reserved.

1. Introduction

Recently, significant interest has been devoted to designing semiconductor–carbon composite materials, aiming at cooperative or synergistic effects between the metal oxides and carbon phases to meet the requirements imposed by specific application, such as solar energy utilization and heterogeneous photocatalysis. Besides the modification of catalysts by incorporating alloying components, the application of appropriate support is another way to improve the performance of catalysts. Various research techniques have been developed and applied towards coating carbon supports for this purpose because a composite product of carbon and semiconductor photocatalysts could potentially create many active sites for photocatalytic degradation [1,2]. Indeed, besides the action as adsorbent or support, some studies have proven that carbon can act as sensitizer and transfer electrons to the semiconductors, triggering the formation of very reactive radicals to improve photocatalytic activity of semiconductors for target reactions. This may be responsible for extending photocatalytic activity

of semiconductors into the visible light range [3–8]. Among carbon supports of similar variety, carbon spheres (CSs) synthesized with an easy hydrothermal approach have aroused considerable interest in a variety of scientific fields because of their wide applications as adsorbents [9], catalysts [10], and electrode materials [11]. Wang et al. [12] have prepared perfect spherical carbon with uniform nanopores by a hydrothermal route, in which sugar was used as carbon sources. In view of environmentally benign and inexpensive properties of carbon spheres [13,14], it would be more meaningful to hydrothermally synthesize effective photocatalysts combined with carbon spheres to further optimize the photocatalytic activity.

The development of visible-light-driven photocatalysts focused on photocatalytic splitting of water or degradation of organic pollutants has inspired a great deal of research interest to utilize solar energy effectively [15–17]. It has been reported that photocatalytic composite oxides containing bismuth such as BiVO₄ (BVO) normally have strong response to visible light due to the change of electronic structure in the composites. BiVO₄ can exist in three crystalline phases, i.e., tetragonal zircon, monoclinic scheelite, and tetragonal scheelite. These three crystal types can undergo phase transition under different thermal conditions [18]. It has been found that BiVO₄ with a monoclinic scheelite structure shows excellent photocatalytic performance under visible light irradiation [17–19].

* Corresponding author. Tel.: +86 571 8898 2032; fax: +86 571 8898 2032.
E-mail addresses: weirong@mail.hz.zj.cn, weirong@zju.edu.cn (W. Zhao).

Compared with TiO_2 photocatalyst, which band gap is 3.2 eV, monoclinic BiVO_4 has a band gap energy of 2.4 eV and can adsorb the solar spectrum up to blue light fraction of ca. 520 nm [20]. Experimental results on the photocatalytic evolution of oxygen [21–23] and the photocatalytic degradation of organic pollutants [24–26] using monoclinic BiVO_4 proved that BiVO_4 was an effective photocatalyst under visible light. Nevertheless, the photocatalytic activity of pure BiVO_4 is limited due to its poor adsorptive abilities and difficult migration of electron–hole pairs [25]. Therefore, it is necessary to find a suitable way like heterostructure fabrication to facilitate the BiVO_4 driven photooxidation of organic pollutants through rapid transfer or separation of photoinduced electron–hole pairs [27].

Copper oxide (CuO), a p-type semiconductor with band gap of 1.70 eV, has been widely used for diverse applications such as heterogeneous catalysts [24,28,29], gas sensors [30,31], lithium ion electrode materials [32,33], and field-emission emitter [34,35]. When copper oxide is in contact with an n-type semiconductor such as BiVO_4 , a p–n-type heterojunction is formed and the recombination of electron–hole pairs is suppressed. Jiang et al. [24] fabricated CuO– BiVO_4 photocatalyst through solution combustion method and impregnation technique, they ascribed the mechanism of enhanced photocatalytic activities to the p-type CuO dispersed on the surface of n-type BiVO_4 to constitute a heterojunction composite, which can separate the electron–hole pairs efficiently.

In this paper, the over goal was to prepare and characterize a class of carbon spheres supported BiVO_4 (BVO@C) by a hydrothermal method towards the photocatalytic oxidation of methylene blue (MB) under visible light irradiation, and finally improve the photocatalytic ability by synthesizing CuO– BiVO_4 (CuO–BVO) heterojunction. Herein, we synthesized carbon-deposited CuO– BiVO_4 (CuO–BVO@C) composite photocatalyst and demonstrated the physical properties and the enhanced photocatalytic activities. The role of carbon spheres and the mechanism underlying the enhanced photocatalytic activity of CuO–BVO@C were also discussed.

2. Experimental

2.1. Photocatalysts preparation

Sucrose, $\text{Bi}(\text{NO}_3)_3 \cdot 5\text{H}_2\text{O}$, NH_4VO_3 , methylene blue, and $\text{Cu}(\text{NO}_3)_2 \cdot 3\text{H}_2\text{O}$ were analytical grade and were used as received without further purification. All the chemicals were supplied from Sinopharm Chemical Reagent (Shanghai, China).

CSs were prepared by a modified hydrothermal synthesis as described in detail elsewhere [36]. Typically, sucrose solution of 0.1 M was filled in a 100 mL stainless steel autoclave with a fill rate of 90%. The autoclave was put into an oven and held at 190 °C for 5 h. After being cooled in air, the product was separated by centrifugation and washed with deionized water and absolute ethanol and finally dried at 80 °C in an oven.

The synthesis process of CuO–BVO@C was as follows: 5 mM $\text{Bi}(\text{NO}_3)_3 \cdot 5\text{H}_2\text{O}$ was dissolved in 20 mL 4 M HNO_3 solution, 0.05 g CSs was then added into the HNO_3 solution and dispersed under magnetic stirring at room temperature for 30 min. Subsequently, a NH_4VO_3 solution, which was prepared by dissolving 5 mM NH_4VO_3 into 20 mL 4 M NaOH solution at 60 °C, was added to the $\text{Bi}(\text{NO}_3)_3$ solution while stirring for 1 h. The 40 mL mixed solution and 35 mL deionized water was then transferred into a Teflon-lined stainless steel autoclave (100 mL in capacity) and hydrothermally reacted at 190 °C for 12 h. After the reaction, the yellow precipitate was filtrated and washed with deionized water and then absolute ethanol for 3–5 times in order to remove any possible impurities. The material was then dried at 100 °C for 2 h to obtain BVO@C catalyst.

Afterwards, The CuO–BVO@C catalyst was prepared by impregnation technique from the aqueous solution of $\text{Cu}(\text{NO}_3)_2 \cdot 3\text{H}_2\text{O}$ as follows, that is, BVO@C catalyst and a suitable copper nitrate solution were mixed in ceramic dish. The molar ratio of CuO to BVO was 5% in CuO–BVO@C composite. The suspension was stirred using a glass rod during evaporation of water on a water bath. Then the dried powder was annealed from 200 °C to 400 °C in a muffle furnace for 4 h to decompose $\text{Cu}(\text{NO}_3)_2 \cdot 3\text{H}_2\text{O}$ to CuO crystallites and then cooled to room temperature. Based on our experiment results (Fig. S1), the CuO–BVO@C sample annealed at 300 °C exhibits the best photocatalytic degradation activity. Therefore, the CuO–BVO@C catalysts unless mentioned in this study were synthesized at 300 °C as the optimal calcinations temperature.

The composite materials were obtained with various loadings of carbon spheres. Catalysts were labeled as xx@yC, where “xx” denotes to BVO or CuO–BVO and “y” is the weight ratio of carbon spheres in a 100 weight basis of neat BVO.

2.2. Characterizations and measurements

The crystal phases of the samples were analyzed by X-ray diffraction (XRD) with Cu K α radiation (model D/max RA, Rigaku, Japan). The accelerating voltage and the applied current were 40 kV and 150 mA, respectively.

The morphology of the samples were investigated by a scanning electron microscopy (SEM, Model S-570, Hitachi, Japan), the nanostructure and crystalline of samples were examined by a transmission electron microscopy (TEM) and a high resolution TEM (HRTEM, JEM-2010, Jeol, Japan) at 200 kV accelerating voltage.

Raman analysis was carried out with Raman spectroscopy (DRX, ThermoFisher, USA) under ambient conditions. The Raman spectra were recorded with a 532 nm laser as the light source.

The Brunauer–Emmett–Teller (BET) surface areas of the sample were obtained from nitrogen adsorption–desorption isotherms determined at liquid nitrogen temperature on an automatic analyzer (Autosorb-iQ-MP, Quantachrome, USA).

The diffuse reflectance spectra (DRS) were obtained for the dry-pressed disk samples using a UV–vis spectrophotometer (TU-1901, Pgeneral, China) equipped with an integrating sphere assembly using BaSO_4 as the reflectance standard. The spectra were recorded in the wavelength ranging from 230 to 800 nm at 25 ± 1 °C.

Photoluminescence spectra (PL) were recorded by a fluorescence spectrophotometer (Fluorolog-3-Tau, France) using a Xe lamp as the excitation light source.

Electrochemical experiments (cyclic voltammetry, Tafel analysis and photocurrent measurements) were carried out with an electrochemical workstation (CH Instruments 650D, Shanghai, China) in a standard three-electrode quartz cell. The indium–tin oxide (ITO) glass was used as the working electrode with BVO, BVO@C, or CuO–BVO@C catalysts via screen printing. A saturated Ag/AgCl electrode and a platinum wire were used as the reference and counter electrode, respectively. The electrolytes were degassed with argon gas for 30 min prior to electrochemical measurements. All potential are reported relative to a saturated Ag/AgCl reference. A 150 W Xe lamp (XQ150 Aojia, Shanghai, China) positioned atop the cell was used as the visible light source. An optical filter (JB420, Jiangsu Haian Education Optical Lens Factory, China) was placed in front of the lamp to allow the passage of light with wavelength longer than 420 nm.

A Bruker model A-300 spectrometer (Bruker instruments, Inc.) equipped with a Xe lamp (with 420 nm filter) was used for measurements of the electron spin-resonance spectroscopy (ESR) signals of radicals spin-trapped by 5,5-dimethyl-1-pyrroline N-oxide (DMPO). The settings were the following: center field 3512 G, microwave frequency 9.86 GHz and power = 20.22 mW.

2.3. Photocatalytic activity tests

The photocatalytic activity of the samples was evaluated by the degradation of MB under visible light irradiation. The activity test procedure was carried out in a 300 mL photocatalytic reactor sealed with quartz plate. A 150 W Xe lamp with a 420 nm optical filter aforementioned was positioned atop the reaction vessel as the visible light source. For a typical photocatalytic experiment, 0.05 g of the as-prepared sample was added into 100 mL of 10 mg L⁻¹ MB solution with constant magnetic stirring. Before illumination, the solution was stirred for 30 min in the dark in order to reach adsorption–desorption equilibrium of MB on the catalysts. Samples were taken at 30 min intervals and centrifuged to remove the photocatalytic particles from the aqueous solution as to obtain the supernatant for the analysis of MB. Then the absorbance of MB was monitored with a UV–vis spectrophotometer aforementioned at 664 nm during the photodegradation process.

3. Results and discussion

3.1. X-ray diffraction

Fig. 1a shows the XRD patterns of the as-prepared BVO, BVO@yC ($y=0.2$ –5.0), and CuO-BVO@1.0C samples. All the

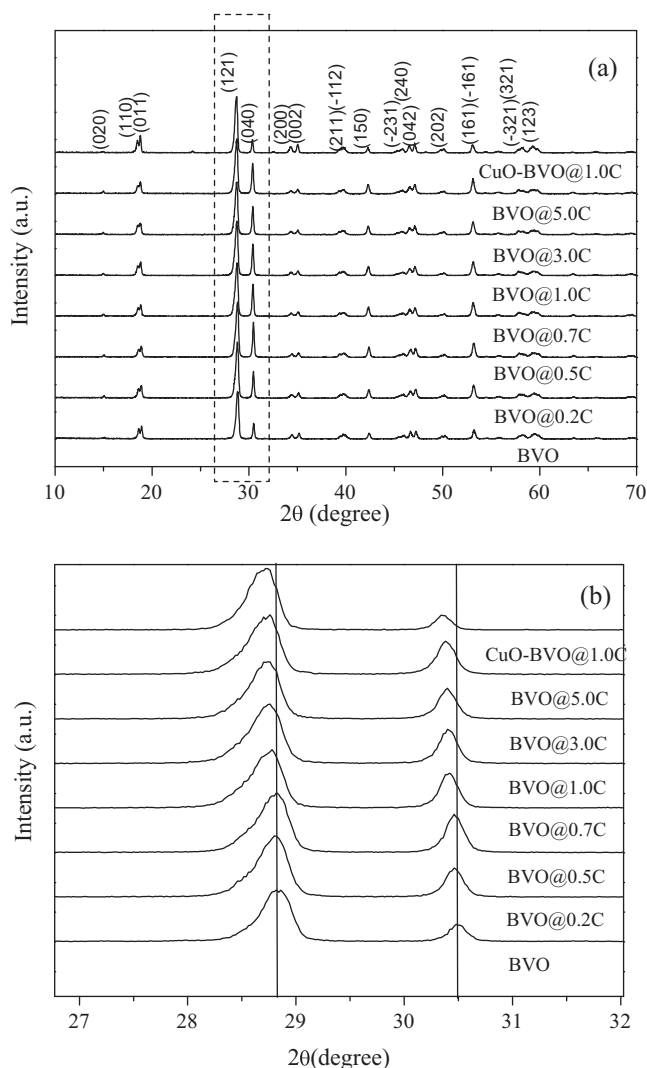


Fig. 1. (a) XRD patterns of BVO, BVO@yC ($y=0.2$ –5.0) and CuO-BVO@1.0C samples, and (b) the details of XRD patterns in the range of 2θ from 27° to 32°.

diffraction peaks in Fig. 1a correspond to the (020), (110), (011), (121), (040), (200), (002), (211), (−112), (150), (−231), (240), (042), (202), (161), (−321), and (123) planes, which can be indexed to the monoclinic scheelite structure of BVO (JCPDS card No. 14-0688, unit-cell parameters $a=5.195$ Å, $b=11.701$ Å, $c=4.092$ Å, $\beta=90.38^\circ$). No diffractive peaks corresponding to CuO were found in CuO-BVO@1.0C composite photocatalyst due to low CuO loading concentration (5 at.%) [37]. The XRD patterns of all these samples present similar profiles, indicating that CSs introduction and CuO loading have no obvious effect on BVO structure. Moreover, no other impurities such as Bi₂O₃ or organic compounds related to reactants were detected, suggesting the phase purity of BVO. The average crystalline sizes of all the samples were estimated from the Scherrer formula as follows:

$$D = \frac{K\lambda}{\sqrt{\beta_s^2 - \beta_e^2} \cos\theta} \quad (1)$$

where D is crystalline size, $K=0.89$ is a coefficient, λ is the X-ray wavelength corresponding to the Cu K α radiation, β_s and β_e are peak widths at half-maximum height of the sample and the equipment broadening, respectively, and $2\theta=28.90^\circ$. The unit-cell parameter of all the prepared samples was analyzed from Bragg equation considering the standard pattern using XRD software accompanying with the equipment. As a result, the crystalline sizes of samples calculated via the Scherrer formula were 286, 280, 276, 272, 270, 267, and 265 Å, respectively. The neat BVO of 286 Å is obtained, while the crystallite sizes of composite catalysts decrease gradually from 280 to 265 Å with the increasing ratios of CSs and BVO. It seems that higher CSs content favors the formation of BVO with smaller crystalline size. This suggests that CSs may act as a dispersing support to suppress the grain growth, favor less extended crystallized BVO domains on CSs surface, and hence avoid BVO particles agglomeration [38]. It is also observed that the corresponding intensities and positions of a few diffraction peaks among the samples are different in some cases. For example, the position of (121) and (040) reflection in BVO@5.0C shows a little shift to lower angle comparing to the others (Fig. 1b), this may be ascribed to the lattice expansion due to the slight portion of carbon atoms incorporation [39], indicating that CSs have a certain influence on the $d(121)$ and $d(040)$ space of BVO during the hydrothermal process. Besides, (121) and (040) reflection in BVO@C samples show higher peak intensity than pure BVO, implying that CSs introduction can lead to a much better crystallinity in the composite catalysts. It has been reported that small grain size and high crystallinity endow higher photocatalytic activity for the increased reactive sites and the promoted electron–hole separation efficiency [40]. Therefore, the as-prepared BVO@C samples are expected to show enhanced photocatalytic performance.

3.2. Scanning and transmission electron microscopy

Fig. 2a shows a SEM image of CSs. As can be seen, large quantities of CSs with an average diameter of ca. 1.2 μ m were produced, which was confirmed by several SEM images at low magnification (data not shown). Perfect spherical shape and uniform particle size can be observed in Fig. 2b and c. Fig. 2d shows a HRTEM image near the edge of the carbon sphere. It reveals that CSs have uneven surfaces and consist of disordered graphene layers on the fringe. The disordered graphene layers on the surface create many defects which provide active site for the bonding of functional groups or metals [41]. The graphitization degree of CSs can be determined by XRD and Raman spectra. The XRD data shown in Fig. 2e are typical of so-called turbostratic carbon in which only the (001) and (hk) are observed due to lacking geometrical correlations between atoms lying in adjacent layers [42]. The peaks appearing at 23.9° and 43.6°

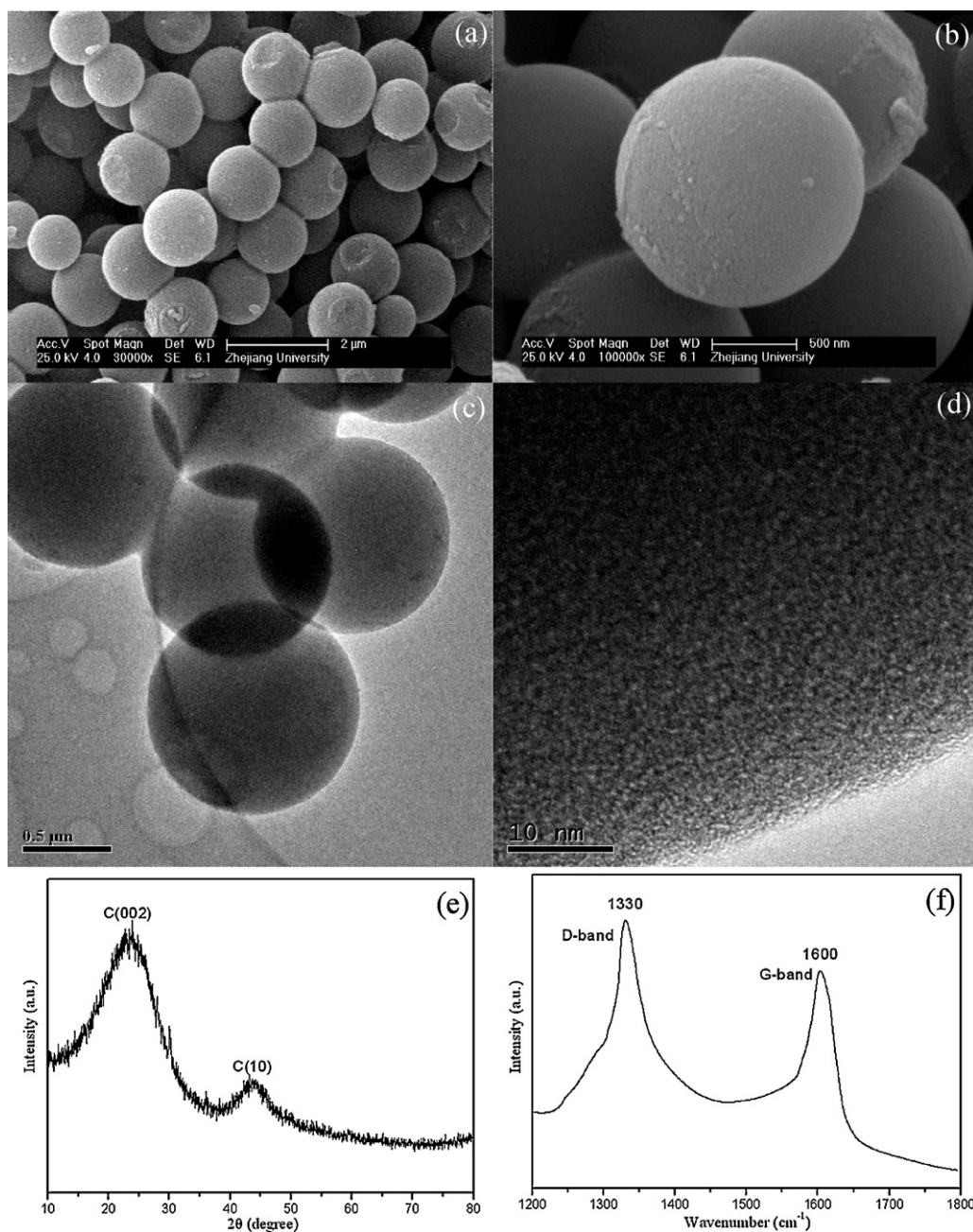


Fig. 2. (a and b) SEM image, (c) TEM image, (d) HRTEM image, (e) XRD patterns, and (f) Raman spectrum of CSs.

can be attributed to the (002) and (10) crystal faces of graphite structure. Furthermore, the broad (10) diffraction originated from a two-dimensional lattice. The peak at 23.9° ($d = 3.72 \text{ \AA}$) shifts to lower angle compared to that of the graphite (26.6° , $d = 3.35 \text{ \AA}$), which indicates that a few graphene layers are stacked without correlations along the c-axis, which could be ascribed to the heavily distorted graphitic structure [42]. The XRD result is in good agreement with that of HRTEM image shown in Fig. 2d and the Raman studies. Fig. 2f shows the Raman spectrum of the as-produced CSs. The Raman band appearing in the wavenumber of 1330 and 1600 cm^{-1} correspond to the D-band and the G-band, respectively. The D-band is associated with vibrations of carbon atoms with dangling bonds in plane terminations of disordered graphite, the G-band is attributed to the ordered graphite structure [43]. The ratio of peak intensity (I_D/I_G) is indicative of the graphitization degree and used to evaluate the defects of carbon material. The ratio of

peak intensity ($I_D/I_G = 1.25$) suggests that the graphitic layers are not well ordered and that there are some defects in the CSs sample.

The microstructures of CuO-BVO@1.0C are shown in Fig. 3. There are no obvious differences in morphology between BVO and CuO-BVO@1.0C, which are both synthesized with the lump-like shape and the size of ca. 500 nm (Fig. 3a). Fig. 3b gives an overview of the typical TEM image of CuO-BVO@1.0C composite particle. The examination of the TEM shows that CuO is gray, whereas BVO is black. Fig. 3c shows the TEM image of the junction for the sample corresponding to the rectangle region of the TEM image in Fig. 3b. A clear and sharp interface can be seen in this figure. Fig. 3d shows the HRTEM image of the sample, which is also from the rectangle region of Fig. 3b. The lower part depicts the (111) plane of CuO with a spacing value of 0.232 nm. The upper part clearly exhibits the BVO (121) facet with a spacing value of 0.308 nm. The clear heterojunction of the sample is revealed. It is also apparent that

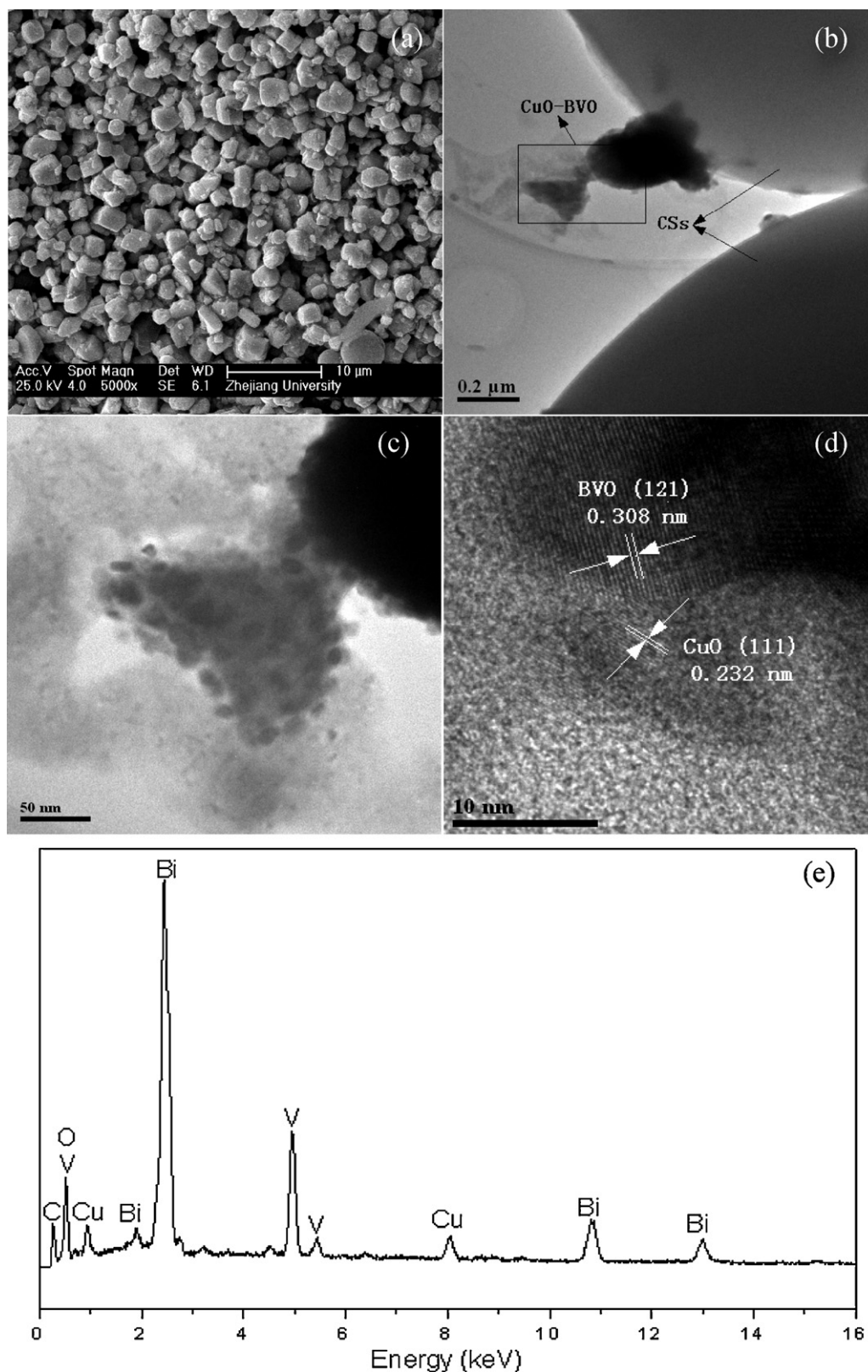


Fig. 3. (a) SEM image, (b and c) TEM images, (d) HRTEM image, and (e) EDX spectrum of CuO-BVO@1.0C according to (a).

Bi, V, Cu, and O elements can be identified from the EDX image (Fig. 3e). Along with FTIR spectra (Fig. S2), it is reasonable to confirm that BVO was truly obtained with hydrothermal method, and a CuO-BVO heterojunction was really formed in the composite catalyst.

The results from BET surface area and average pore diameter measurements for the samples are also given in Table S1. When CSs are composited with BVO, the S_{BET} and pore size increase gradually along with the increasing CSs content. The S_{BET} of CuO-BVO@1.0C composite is $4.06 \text{ m}^2 \text{ g}^{-1}$, which is larger than that of BVO@1.0C

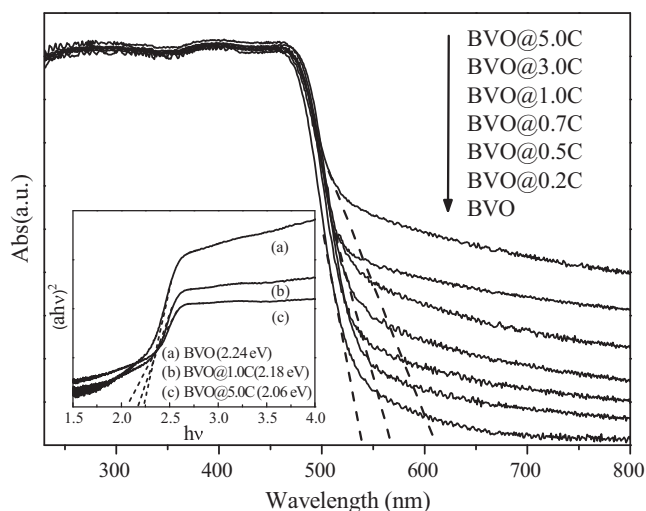


Fig. 4. UV-vis diffuse reflectance spectra of BVO and BVO@yC ($y = 0.2–5.0$) samples. The inset shows the band gap evaluation for linear dependence of $(\alpha h\nu)^2$ versus $h\nu$ for the BVO, BVO@1.0C, and BVO@5.0C samples.

($2.86 \text{ m}^2 \text{ g}^{-1}$). This enlarged S_{BET} is attributed to introducing the nanoparticles CuO on the surface of BVO.

3.3. UV-vis diffuse reflection spectra

Fig. 4 shows the diffuse reflectance spectra of BVO and BVO@yC ($y = 0.2–5.0$) samples. All light absorbance profiles have a trailing edge in 450–510 nm indicating direct band gap of the semiconductors [44]. It is also noted that each sample shows different absorption profile in visible light region except for that of strong absorption in the UV-light region. It could be seen that BVO has no evident absorption in the region of 550–800 nm, but BVO@C samples have obvious absorption between 550 and 800 nm, which enhanced with the increase of CSs content in the composite catalysts, while the powder shifts from vivid yellow to green yellow with increasing CSs content. As for this extension of absorption range, it could be attributed to the relation of induced interphase interaction between BVO and CSs, the analogous observations of semiconductor coated with carbonaceous species were also experimentally reported in some other systems [6,45]. Additionally, these observations might indicate an increment of surface electric charge of BVO in the composite catalysts due to CSs introduction [3]. In other words, CSs may be considered as photosensitizer which may contribute to modifications of the fundamental process of electron transfer when irradiated by visible light [46–48].

The band gaps of samples can be estimated based on the diffuse reflection spectral data [49], the relation between absorption coefficient (α) and incident photon energy ($h\nu$) can be expressed as $\alpha h\nu = B_i(h\nu - E_g)^n$, where B_i is the absorption constant, E_g is the band gap energy (eV), $n = 0.5$ for direct and 2 for indirect transition. Plots of $(\alpha h\nu)^2$ versus $h\nu$ from the spectral data are presented in the inset of Fig. 4. The direct band gaps of BVO, BVO@1.0C, and BVO@5.0C samples are estimated to be 2.24, 2.18, and 2.06 eV, respectively. They are slightly smaller than the reported values of pure BVO [18,27,50], which could be attributed to large particle sizes, surface defects or small amount of carbon incorporation. The decrease in band gap energy indicates that BVO@C has a much greater optical absorption region than pure BVO, which can be excited to produce more electron–hole pairs under the same visible light illumination and then result in higher photocatalytic activity. In addition, there is no apparent difference of band gap absorption edge between BVO@1.0C and CuO-BVO@1.0C (profile not given), suggesting the decrease of band gap energy is mainly affected by

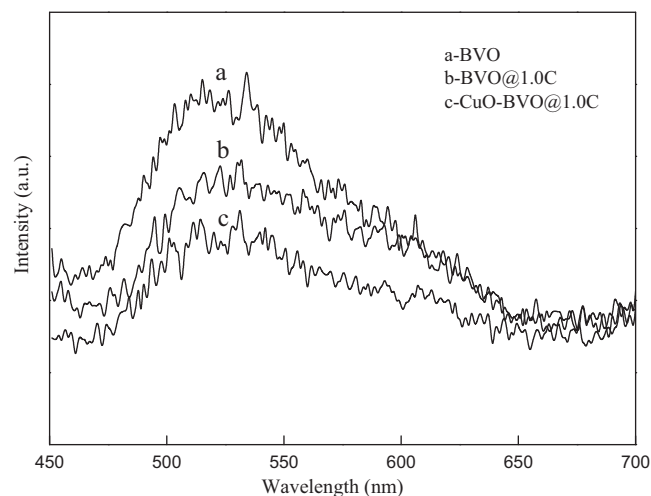


Fig. 5. Photoluminescence spectra of samples (a) BVO, (b) BVO@1.0C, and (c) CuO-BVO@1.0C.

CSs in comparison with CuO-BVO heterojunction. The reason could be due to the fact that CuO concentration is so low in the composite catalyst that it can barely influence on the change of band gap.

3.4. Photoluminescence spectra

PL emission spectra are often used to disclose the immigration, transfer, and recombination processes and to understand the fate of electron–hole pairs in semiconductor particles [51]. With electron–hole pair recombination after a photocatalyst irradiated (i.e. laser), photons are emitted, resulting in photoluminescence. Fig. 5 shows the comparison of PL spectra with 370 nm excitation wavelength for BVO, BVO@1.0C and CuO-BVO@1.0C catalysts at room temperature. All of the PL spectra are observed at around 540 nm and the PL intensity decreases as: BVO > BVO@1.0C > CuO-BVO@1.0C. It can be clearly observed that BVO@1.0C shows diminished PL intensity in comparison to pure BVO indicating reduced charge carrier recombination. This may be ascribed to the increase in trap states on surface defect of BVO with the assistance of CSs [52], which is in accordance with HRTEM (Fig. 3) and DRS (Fig. 4) results. In addition, it has been confirmed that photoinduced charge transfer occurs in the electronic interaction between the semiconductors (or polymers chains) with carbon materials [4,53]. Since there is an interaction between BVO and CSs and they connect well with each other (Fig. 3), we propose that electron transfer also happens in the BVO@1.0C composites, leading to the reduction of electron–hole pairs and the increase in photon efficiency. As for CuO-BVO@1.0C, a decrease in PL intensity is also observed as compared to BVO@1.0C. The results clearly show that the recombination of photogenerated charge carrier is inhibited greatly by the presence of small quantity CuO, leading to the weak recombination of electron–hole pairs and high photon efficiency, and the photocatalytic reaction will be enhanced accordingly. This result shows good agreement with the analysis by the energy band position of the p–n heterojunction semiconductors (Table S2).

3.5. Photocurrent density measurement

Photocurrent density was measured to evaluate the charge separation capability of heterojunction as-prepared under visible light irradiation. Fig. 6 shows the different effects of bias potentials on photocurrent density for BVO@1.0C and CuO-BVO@1.0C. The photocurrent density of BVO@1.0C increases with the applied potential in the range of -0.15 to 0.25 V, and the photocurrent density with

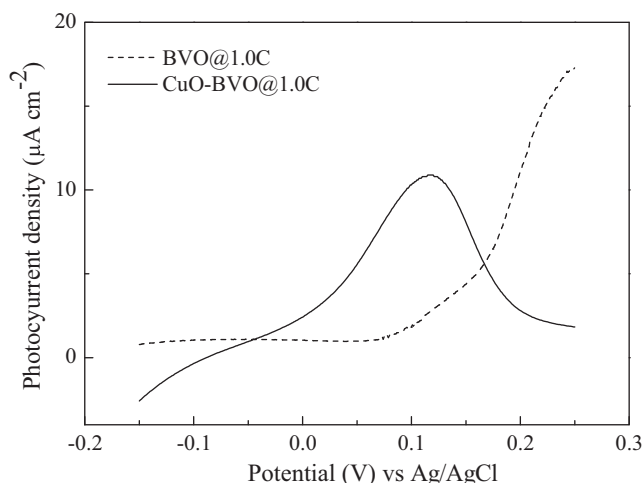


Fig. 6. Photocurrent density versus potential plotted for BVO@1.0C and CuO-BVO@1.0C electrodes in 0.01 M Na_2SO_4 under visible light irradiation.

a bias potential of more than 0.2 V is apparently higher than the maximal photocurrent density of CuO-BVO@1.0C, so the effective quantity of BVO in CuO-BVO@1.0C is less than that in BVO@1.0C. However, the photocurrent density of CuO-BVO@1.0C is larger than that of BVO@1.0C at the same potential from -0.04 to 0.17 V. When the applied potential increases from -0.15 to 0.12 V, the photocurrent density of CuO-BVO@1.0C increases gradually until reaching its maximum, $10.90 \mu\text{A cm}^{-2}$, and then it begins to decline. It could be attributed to that photogenerated electrons and holes are separated by the interior electric field of space charge layer in the heterojunction system, however, with the increase of bias potential, the driving force for separation of holes and electrons is weakened due to the thinning of the space charge layer, leading to the decrease of photocurrent [54].

3.6. Cyclic voltammetry and Tafel characterization

Cyclic voltammetry and Tafel analysis were adopted to assess the electrocatalytic capability of the catalysts under visible light illumination. Fig. 7 shows cyclic voltammograms obtained at scan rate of 10 mV s^{-1} in a solution of $1.0 \text{ mM K}_4\text{Fe}(\text{CN})_6$ and

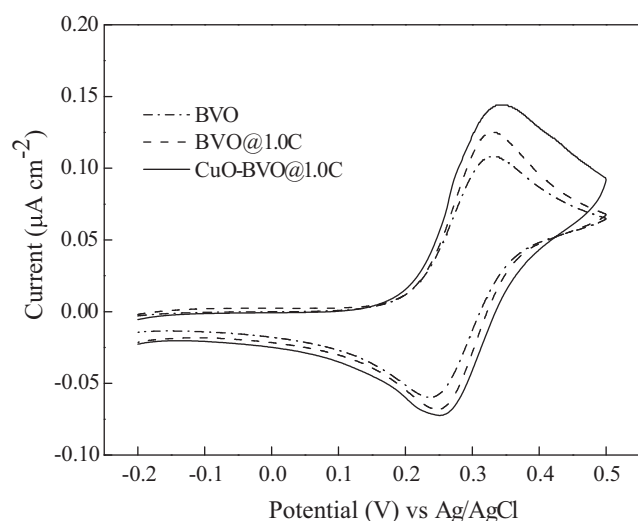


Fig. 7. Cyclic voltammograms of the various electrodes in a solution of $1.0 \text{ mM K}_4\text{Fe}(\text{CN})_6$ and 1.0 M KCl at scan rate of 10 mV s^{-1} under visible light irradiation: (a) BVO, (b) BVO@1.0C, and (c) CuO-BVO@1.0C.

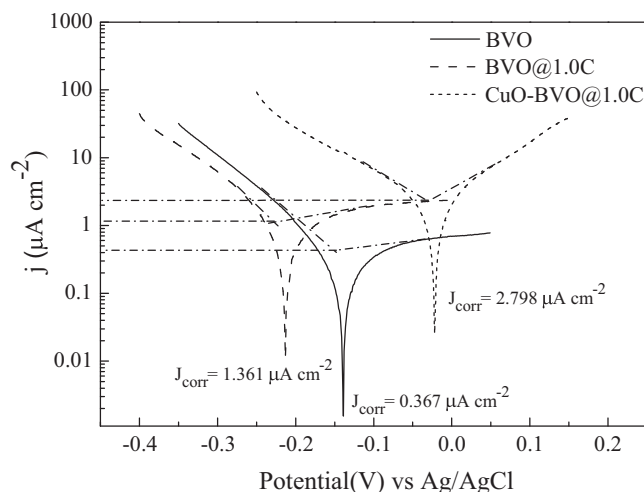


Fig. 8. Tafel polarization curves of the various electrodes in $0.1 \text{ M Na}_2\text{SO}_4$ solution at scan rate of 5 mV s^{-1} under visible light irradiation: (a) BVO, (b) BVO@1.0C, and (c) CuO-BVO@1.0C.

1.0 M KCl , which usually serves as a benchmark for investigating electrocatalytic properties of different carbon structures [10,55,56]. As depicted, all three electrodes show in general apparent reversibility voltammograms. The results also show that the $\text{Fe}(\text{CN})_6^{4-}/\text{Fe}(\text{CN})_6^{3-}$ redox pairs is highly resolved at the CuO-BVO@1.0C electrode at which the redox current is 1.35-fold as great as that at the BVO electrode. It is evidently observed that redox current increases considerably and peak-to-peak separation reduces slightly in the order of BVO, BVO@1.0C, and CuO-BVO@1.0C electrodes, and it is apparent that the electron-transfer kinetics at the CuO-BVO@1.0C electrode has been fostered compared to other catalysts by the decreased overpotential required to oxidize the ferrocyanide. This also suggests that the addition of CSs to BVO enhances the interaction not only among BVO particles, but also between the BVO and the ITO substrate [57]. Furthermore, the peak-to-peak separation is an indication of the heterogeneous charge transfer kinetics further showing that CuO-BVO@1.0C exhibit fast electron transfer [58]. Tafel analysis allows a clear and pictorial view of the current density value for the system under investigation. Tafel curves and the corrosion current density J_{corr} determined by extrapolating the linear portions of the anodic and cathodic Tafel regions to their point of intersection are shown in Fig. 8. The J_{corr} of BVO@1.0C and CuO-BVO@1.0C is 1.361 and $2.798 \mu\text{A cm}^{-2}$, which are approximately four and eight times higher than that of BVO, respectively. It is also noted that CuO-BVO@1.0C shows largest anodic Tafel slope as compared with BVO and BVO@1.0C. The larger J_{corr} and the anodic Tafel slope show that CuO-BVO@1.0C is more reactive, indicating the good electrocatalytic performance and faster electron transfer. All these electrochemical results might demonstrate that CSs may act as electron sensitizer and donators in the composite photocatalysts to accept the photoinduced electron generated from light irradiation, leading to higher photocurrent response and favorable for electronic transfer.

3.7. Photocatalytic activity

Fig. 9 shows the photocatalytic performance (C/C_0) versus visible light irradiation time of the as-fabricated samples for MB degradation in an aqueous solution. The experimental results (Fig. S3) confirm that the optimum loading ratio of CSs and BVO is 1.0 wt\% . For comparison purposes, we conducted the experiments of MB degradation over BVO, CuO-BVO, BVO@1.0C and CuO-BVO@1.0C catalysts under identical conditions and the results were shown in Fig. 9. The direct photolysis of MB is ca. 8% after 3 h

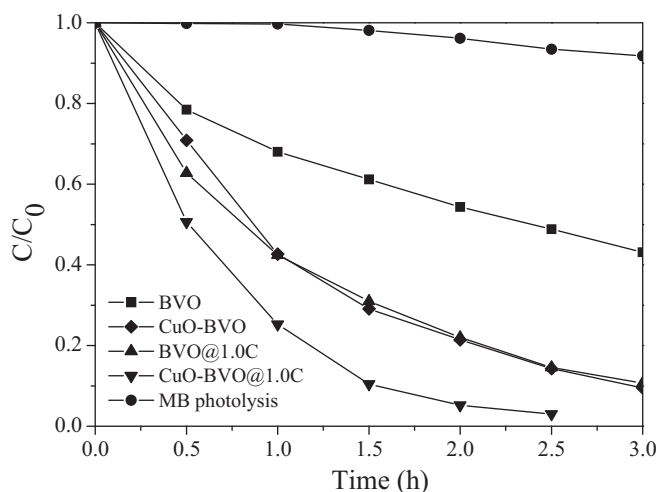


Fig. 9. Photocatalytic activities of BVO, BVO@1.0C, and CuO-BVO@1.0C samples for the degradation rate of MB at initial concentration of 10 mg L^{-1} under visible light irradiation.

irradiation, demonstrating that the self-degradation of MB is rather slow. However, it is clearly demonstrated that CuO-BVO@1.0C shows the highest photocatalytic degradation activity of MB (ca. 100% within the reaction of 2.5 h) because its degradation rate in C/C_0 is the fastest among the four samples.

Wang et al. [59] revealed the following pseudo-first-order reaction kinetics can be used to describe the initial MB degradation rate of heterogeneous photocatalytic oxidation process.

$$-\frac{dC}{dt} = K_a C \quad (2)$$

where C is the MB concentration (mg L^{-1}) at time t (h), K_a is the observed pseudo-first-order rate constant. K_a can then be determined by fitting the pseudo-first-order rate expression from Eq. (2) to the experimental data. K_a has been chosen as the basic kinetic parameter for the different photocatalysts, since it enables one to determine a photocatalytic activity independent of the previous adsorption period in the dark and the concentration of solute remaining in the solution. The calculated K_a values of BVO, CuO-BVO, BVO@1.0C, and CuO-BVO@1.0C are 0.298, 0.786, 0.765, and 1.439 h^{-1} , respectively. Obviously, CuO-BVO@1.0C has the highest rate constant among four samples, approximately two and five times higher than BVO and BVO@1.0C, respectively. The enhanced photocatalytic activity over the CuO-BVO@1.0C composite catalyst may be attributed to obviously low recombination rate of electron-hole pairs, high yield of electron-hole pairs, and fast electron transfer rate due to the presence of CSs and CuO. Therefore, the synergistic effect between heterojunction structure and CSs would account for the excellent photocatalytic activity of CuO-BVO@C catalysts.

The absorption spectral change in the concentration of MB using CuO-BVO@1.0C as photocatalyst is shown in Fig. S4. It can be seen that the λ_{max} gradually shifts from 664 to 651 nm with the decrease in absorbance during the visible light irradiation. The blue shifts from 654 to 651 nm are attributed to the N -demethylation of MB, and the formation of N,N,N' -trimethylated azure B (AB).

3.8. Performance of recycled catalyst

The stability and reusability of catalysts are very important issues for practical applications. The CuO-BVO@1.0C catalyst was reused in four successive photoreaction experiments by simple filtration after reaction. Fig. 10 shows results of four successive MB degradation runs using the reclaimed CuO-BVO@1.0C catalyst

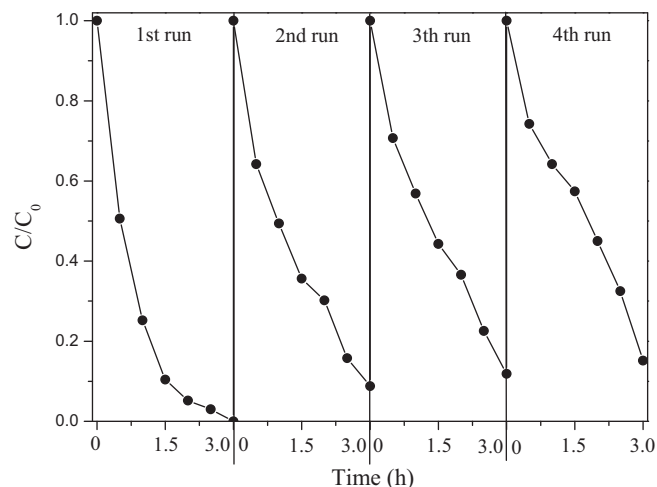


Fig. 10. Cycling runs in the photocatalytic degradation of MB in the presence of CuO-BVO@1.0C sample at initial concentration of 10 mg L^{-1} under visible light irradiation.

while keeping the experimental conditions unchanged. It can be seen that the catalyst does not exhibit a significant loss of activity in four successive runs. MB removal remains higher than 85% in each cycle, confirming CuO-BVO@1.0C is not photocorroded and rather stable during the photocatalytic oxidation of MB. This novel composite catalyst is promising for practical application in water purification and it is another prerequisite in comparison with doped TiO_2 , which sometimes suffers from an instability problem.

3.9. ESR measurement

The generation of $\cdot\text{O}_2^-$ and $\cdot\text{OH}$ radicals in the photocatalytic process have been confirmed by the ESR spin-trap with DMPO technique, and the result was shown in Fig. 11. No ESR signals were detected when the reaction was performed in the dark. However, under visible irradiation four characteristic peaks of DMPO- $\cdot\text{OH}$ can be obviously observed in the suspension of CuO-BVO@1.0C catalyst, while the ESR signals of DMPO- $\cdot\text{O}_2^-$ adducts with characteristic six peaks can be observed under visible irradiation in CuO-BVO@1.0C methanolic dispersions [60]. This results provide a strong indication that the photogenerated charge carriers in a CuO-BVO@1.0C photocatalyst not only possess strong redox ability but also are long-lived enough to react with the surface adsorbed O_2 or H_2O to produce $\cdot\text{OH}$ radicals. The generated $\cdot\text{OH}$ plays a pivotal role and is recognized as the main reactive species responsible for the degradation of pollutants.

3.10. Electron transfer mechanism

It is well known that the light absorption capability of photocatalyst and separation of excited electron-hole pairs are crucial factors influencing the photoactivity. From all experimental results mentioned above, a possible mechanism for photodegradation of MB over CuO-BVO@C composite catalyst has been proposed as illustrated in Fig. 12. The CSs effect on the activity of BVO can be explained in terms of its action as dispersing agent and photosensitizer, respectively. However, the role CSs as photosensitizer is more likely to be the key factor accounting for enhanced photocatalytic activity which is clearly observed in DRS, PL and electrochemistry characterizations. As photosensitizer, CSs may absorb the irradiation and inject the photogenerated electrons into the conduction band of CuO or BVO (Eq. (3)), then the rate of electron transfer to oxygen adsorbed on the catalyst surface increases. Simultaneously, the positively charged CSs might remove an

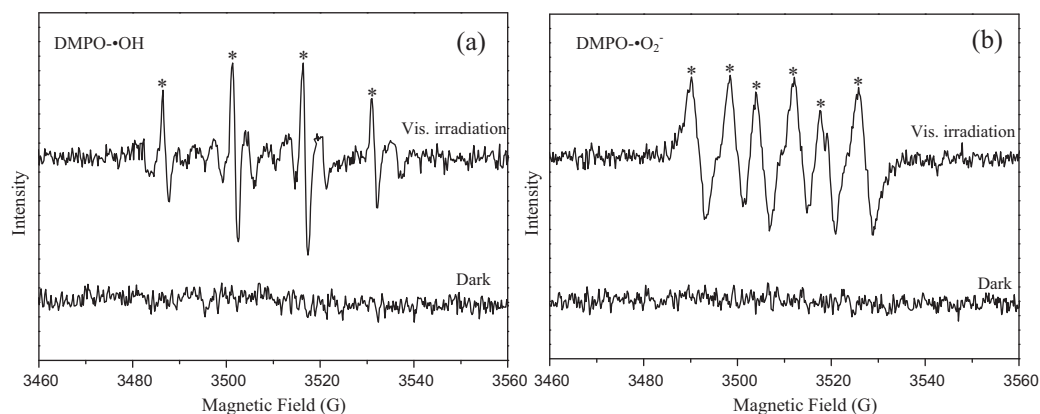
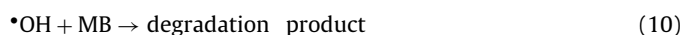
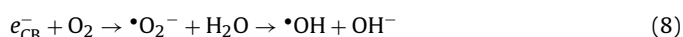


Fig. 11. DMPO spin-trapping ESR spectra for CuO-BVO@1.0C sample: (a) in aqueous dispersion for DMPO-•OH and (b) in methanol dispersion for DMPO-•O₂⁻.

electron from the valence band of BVO leaving a hole (Eq. (5)). Also, in the p–n-type heterojunction structure of CuO-BVO, an internal field will be formed with the direction from n-type semiconductor to p-type semiconductor at the thermodynamic equilibrium [24]. According to the predicted position of band energy from our experiment listed in Table S1, the excited electrons on the conduction band of the p-type CuO semiconductor are prohibited to transfer to the conduction band of n-type BVO semiconductor by the energy barrier existed at the interface between CuO and BVO crystallites (Eq. (6)) [24]. While the excited holes on the valence band of BVO semiconductor will be readily transferred to the valence band of CuO semiconductor (Eq. (7)). Consequently, the separation of photogenerated electron–hole pairs on the BVO semiconductor would be enhanced and the recombination rate could be inhibited. The photoinduced electrons in the composite catalyst are then captured by O₂, triggering the formation of a very reactive superoxide radical ion (•O₂⁻) (Eqs. (4) and (8)). Simultaneously, the resulted holes can then react with the OH⁻ derived from H₂O and form a hydroxyl radical •OH (Eq. (9)). The generated •O₂⁻ would further interact with H₂O adsorbed to produce more •OH radicals (Eq. (8)). These radicals group are responsible for the decomposition of organic compounds (MB) (Eq. (10)).



4. Conclusions

In this study, we present the synthesis and characterization of CuO-BVO@C composite catalyst through hydrothermal method and impregnation technique. The XRD patterns reveal that all prepared catalysts exhibit the typical monoclinic scheelite BVO without CuO phase detected, and higher CSs content favors the formation BVO with smaller crystalline size. The SEM images show that CSs are spherical particles and quite uniform with a narrow size distribution (ca. 1.2 μm). CuO-BVO heterojunction is confirmed by TEM-EDX analysis and photocurrent measurement, and the formed CuO-BVO is dispersed over the edge of large CSs particles. The diagrams of DRS demonstrate that all the BVO@C catalysts show the absorption in the visible region between 550 and 800 nm and the absorption intensity increases with the increase of CSs content. It is also found that CSs introduction could effectively narrow down the band gap of the catalysts. PL spectra further confirm that the recombination of photogenerated charge carrier can be inhibited greatly in the presence of CSs and CuO, leading to the increasing of photon efficiency. Cyclic voltammograms and Tafel curves show that CuO-BVO@C exhibits excellent electrocatalytic performance, such as strong photocurrent response and fast electronic transfer. The photocatalytic activities results indicate that CuO-BVO@C exhibits the best photocatalytic activity with K_a value five times higher than pure BVO for decomposition of MB under visible light irradiation. The active species •O₂⁻ and •OH radicals were detected by ESR technology and proved to be the most important reason for the photodegradation of organic pollutant. The enhanced photocatalytic performance of CuO-BVO@C may be attributed to not only interconnected heterojunction of CuO-BVO but also carbon spheres sensitization. The presence of carbon spheres in the composite of CuO-BVO@C plays two important roles. One is to act as a dispersing support to affect the grain growth, the other role is to act as a photosensitizer to transfer electrons to CuO-BVO, which narrows the band gap of BVO, hinders the recombination of electron–hole pairs, extends the absorption range of visible light, and improves the photocatalytic performance of catalyst. Accordingly, a reasonable mechanism was proposed to explain the role of carbon spheres in the CuO-BVO@C composites as a photocatalyst for degradation of organic pollutants.

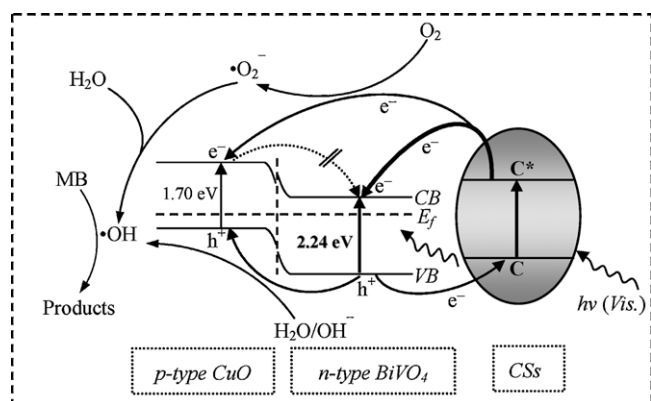


Fig. 12. A proposed visible light photodegradation mechanism of organic compounds over CuO-BVO@C photocatalyst.

Acknowledgments

This work has been partially supported by National Nature Science Foundation of China (grant no. 51178412), Zhejiang Provincial Natural Science Foundation of China (grant no. Y5090149), Zhejiang Provincial Education Department Scientific Research Projects (grant no. Z201122663), and the National Water Pollution Control and Management Project of China (2011ZX07101-012).

Appendix A. Supplementary data

Supplementary data associated with this article can be found, in the online version, at doi:10.1016/j.apcatb.2011.12.018.

References

- [1] Y.J. Xu, Y.B. Zhuang, X.Z. Fu, J. Phys. Chem. C 114 (2010) 2669–2676.
- [2] M.L. Chen, C.S. Lim, W.C. Oh, J. Ceram. Process. Res. 8 (2007) 119–124.
- [3] W.D. Wang, P. Serp, P. Kalck, J.L. Faria, J. Mol. Catal. A: Chem. 235 (2005) 194–199.
- [4] W.C. Oh, A.R. Jung, W.B. Ko, Mater. Sci. Eng. C 29 (2009) 1338–1347.
- [5] O. Akhavan, M. Abdollahi, Y. Abdi, S. Mohajezadeh, Carbon 47 (2009) 3280–3287.
- [6] Y. Ou, J.D. Lin, S.M. Fang, D.W. Liao, Chem. Phys. Lett. 429 (2006) 199–203.
- [7] F. Dong, W.R. Zhao, Z.B. Wu, Nanotechnology 19 (2008) 365607.
- [8] K. Woan, G. Pyrgiotakis, W. Sigmund, Adv. Mater. 21 (2009) 2233–2239.
- [9] S.X. Liu, J. Sun, Z.H. Huang, J. Hazard. Mater. 173 (2010) 377–383.
- [10] J. Wu, F.P. Hu, X.D. Hu, Z.D. Wei, P.K. Shen, Electrochim. Acta 53 (2008) 8341–8345.
- [11] Z.H. Yi, Y.G. Liang, X.F. Lei, C.W. Wang, J.T. Sun, Mater. Lett. 61 (2007) 4199–4203.
- [12] Q. Wang, H. Li, L.Q. Chen, X.J. Huang, Carbon 39 (2001) 2211–2214.
- [13] Y.L. Min, Y. Wan, R. Liu, S.H. Yu, Chin. J. Inorg. Chem. 24 (2008) 1172–1176.
- [14] Y.Y. Li, J.P. Liu, X.T. Huang, J.G. Yu, Dalton Trans. 39 (2010) 3420–3425.
- [15] H.G. Kim, P.H. Borse, W.Y. Choi, J.S. Lee, Angew. Chem. Int. Ed. 44 (2005) 4585–4589.
- [16] H.M. Liu, R. Nakamura, Y. Nakato, Chemphyschem 6 (2005) 2499–2502.
- [17] S. Kohtani, J. Hiro, N. Yamamoto, A. Kudo, K. Tokumura, R. Nakagaki, Catal. Commun. 6 (2005) 185–189.
- [18] S. Tokunaga, H. Kato, A. Kudo, Chem. Mater. 13 (2001) 4624–4628.
- [19] H.M. Liu, R. Nakamura, Y. Nakato, J. Electrochem. Soc. 152 (2005) G856–G861.
- [20] A. Kudo, K. Omori, H. Kato, J. Am. Chem. Soc. 121 (1999) 11459–11467.
- [21] A. Kudo, K. Ueda, H. Kato, I. Mikami, Catal. Lett. 53 (1998) 229–230.
- [22] D.N. Ke, T.Y. Peng, L. Ma, P. Cai, K. Dai, Inorg. Chem. 48 (2009) 4685–4691.
- [23] S.S. Dunkle, R.J. Helmich, K.S. Suslick, J. Phys. Chem. C 113 (2009) 11980–11983.
- [24] H.Q. Jiang, H. Endo, H. Natori, M. Nagai, K. Kobayashi, Mater. Res. Bull. 44 (2009) 700–706.
- [25] M. Long, W.M. Cai, J. Cai, B.X. Zhou, X.Y. Chai, Y.H. Wu, J. Phys. Chem. B 110 (2006) 20211–20216.
- [26] W.Z. Yin, W.Z. Wang, L. Zhou, S.M. Sun, L. Zhang, J. Hazard. Mater. 173 (2010) 194–199.
- [27] D.K. Lee, I.S. Cho, S. Lee, S.T. Bae, J.H. Noh, D.W. Kim, K.S. Hong, Mater. Chem. Phys. 119 (2010) 106–111.
- [28] Z.L. Jin, X.J. Zhang, Y.X. Li, S.B. Li, G.X. Lu, Catal. Commun. 8 (2007) 1267–1273.
- [29] T.L. Hsiung, H.P. Wang, Y.M. Lu, M.C. Hsiao, Radiat. Phys. Chem. 75 (2006) 2054–2057.
- [30] A. Chowdhuri, V. Gupta, K. Sreenivas, R. Kumar, S. Mozumdar, P.K. Patanjali, Appl. Phys. Lett. 84 (2004) 1180–1182.
- [31] J. Herran, G.G. Mandayo, I. Ayerdi, E. Castano, Sens. Actuators B: Chem. 129 (2008) 386–390.
- [32] P. Poizot, S. Laruelle, S. Grugeon, L. Dupont, J.M. Tarascon, Nature 407 (2000) 496–499.
- [33] W.Z. Xiong, G.M. Kale, Sens. Actuators B: Chem. 119 (2006) 409–414.
- [34] J. Chen, S.Z. Deng, N.S. Xu, W.X. Zhang, X.G. Wen, S.H. Yang, Appl. Phys. Lett. 83 (2003) 746–748.
- [35] C.T. Hsieh, J.M. Chen, H.H. Lin, H.C. Shih, Appl. Phys. Lett. 83 (2003) 3383–3385.
- [36] S.C. Tang, Y.F. Tang, S. Vongehr, X.N. Zhao, X.K. Meng, Appl. Surf. Sci. 255 (2009) 6011–6016.
- [37] C.L. Yu, K. Yang, J.C. Yu, F.F. Cao, X. Li, X.C. Zhou, J. Alloys Compd. 509 (2011) 4547–4552.
- [38] W.D. Wang, P. Serp, P. Kalck, J.L. Faria, Appl. Catal. B: Environ. 56 (2005) 305–312.
- [39] C. Di Valentin, G. Pacchioni, A. Selloni, Chem. Mater. 17 (2005) 6656–6665.
- [40] J.G. Yu, J.F. Xiong, B. Cheng, S.W. Liu, Appl. Catal. B: Environ. 60 (2005) 211–221.
- [41] Z.C. Kang, Z.L. Wang, J. Phys. Chem. 100 (1996) 5163–5165.
- [42] H.C. Wu, C.T. Hong, H.T. Chiu, Y.Y. Li, Diam. Relat. Mater. 18 (2009) 601–605.
- [43] F. Tuinstra, J.L. Koenig, J. Phys. Chem. 53 (1970) 1126.
- [44] B. Zhou, X. Zhao, H.J. Liu, J.H. Qu, C.P. Huang, Appl. Catal. B: Environ. 99 (2010) 214–221.
- [45] C. Lettmann, K. Hildenbrand, H. Kisch, W. Macyk, W.F. Maier, Appl. Catal. B: Environ. 32 (2001) 215–227.
- [46] X. Yang, C. Cao, K. Hohn, L. Erickson, R. Maghirang, D. Hamal, K. Klabunde, J. Catal. 252 (2007) 296–302.
- [47] C. Lettmann, K. Hildenbrand, H. Kisch, W. Macyk, W.F. Maier, Appl. Catal. B 32 (2001) 215–227.
- [48] J. Zhong, F. Chen, J. Zhang, J. Phys. Chem. C 114 (2010) 933–939.
- [49] H. Lin, C.P. Huang, W. Li, C. Ni, S.I. Shah, Y.H. Tseng, Appl. Catal. B: Environ. 68 (2006) 1–11.
- [50] H.Q. Jiang, M. Nagai, K. Kobayashi, J. Alloys Compd. 479 (2009) 821–827.
- [51] H. Yamashita, Y. Ichihashi, S.G. Zhang, Y. Matsumura, Y. Souma, T. Tatsumi, M. Anpo, Appl. Surf. Sci. 121 (1997) 305–309.
- [52] S. Shamaia, A.K.L. Sajjad, F. Chen, J.L. Zhang, Appl. Catal. B: Environ. 94 (2010) 272–280.
- [53] Y. Yu, J.C. Yu, J.G. Yu, Y.C. Kwok, Y.K. Che, J.C. Zhao, L. Ding, W.K. Ge, P.K. Wong, Appl. Catal. A: Gen. 289 (2005) 186–196.
- [54] H.T. Yu, X. Quan, S. Chen, H.M. Zhao, J. Phys. Chem. C 111 (2007) 12987–12991.
- [55] R.Z. Yang, X.P. Qiu, H.R. Zhang, J.Q. Li, W.T. Zhu, Z.X. Wang, X.J. Huang, L.Q. Chen, Carbon 43 (2005) 11–16.
- [56] Z. Hamoudi, B. Aissa, M.A. El Khakani, M. Mohamedi, J. Phys. Chem. C 114 (2010) 1885–1891.
- [57] C. Dechakiatkrai, J. Chen, C. Lynam, S. Phanichphant, G.G. Wallace, J. Electrochem. Soc. 154 (2007) A407–A411.
- [58] C.E. Banks, R.R. Moore, T.J. Davies, R.G. Compton, Chem. Commun. (2004) 1804–1805.
- [59] X.H. Wang, J.G. Li, H. Kamiyama, Y. Moriyoshi, T. Ishigaki, J. Phys. Chem. B 110 (2006) 6804–6809.
- [60] H.B. Fu, L.W. Zhang, S.C. Zhang, Y.F. Zhu, J.C. Zhao, J. Phys. Chem. B 110 (2006) 3061–3065.